Three-Dimensional Seismic Velocity Models for Alaska from Joint Tomographic Inversion of Body-Wave and Surface-Wave Data

by Avinash Nayak[1*], Donna Eberhart-Phillips[2], Natalia A. Ruppert[3], Hongjian Fang[4], Melissa M. Moore[5], Carl Tape[3], Douglas H. Christensen[3], Geoffrey A. Abers[6], Clifford H. Thurber[1]

June 9, 2020

For submission to SRL

[*]Department of Geoscience, University of Wisconsin-Madison, 1215 W. Dayton St., Madison, WI, USA 53706 (avinash07guddu@gmail.com)

[1]Department of Geoscience, University of Wisconsin-Madison, Madison, Wisconsin, USA

[2]Department of Earth and Planetary Sciences University of California, Davis; and GNS Science, Dunedin, New Zealand

[3]Geophysical Institute, University of Alaska Fairbanks

[4]Department of Earth, Atmospheric and Planetary Sciences, Massachusetts Institute of Technology

[5]Department of Physics and Earth Science, University of North Alabama

[6]Department of Earth and Atmospheric Sciences, Cornell University

Abstract We present new state-wide seismic velocity models for Alaska from joint inversions of body-wave and surface-wave data using two different methods. Our work takes advantage of data from many recent temporary seismic arrays, including the IRIS Alaska Transportable Array. Our model results for three-dimensional compressional- and shear-wave velocity and their ratio are generally consistent with previous studies, but provide higher-resolution images in many areas than were available previously, especially in sedimentary basins. We also find that the depth to the subducting Pacific Plate beneath southern Alaska appears to be deeper than previous models.

Introduction

There is a long history of large-scale seismic tomography studies of the three-dimensional (3-D) structure of Alaska, especially regarding its subduction zone. Among the body-wave tomography studies that pre-date the availability of data from the EarthScope Alaska Transportable Array (ATA) are regional earthquake tomography studies of P-wave velocity (Vp) (Kissling and Lahr, 1991; Zhao *et al*., 1995; Qi *et al*., 2007), Vp and the ratio of Vp to shear wave velocity Vs (Vp/Vs) (Eberhart-Phillips *et al*., 2006; van Stiphout *et al*., 2009), Vp, Vs, and P-wave anisotropy (Tian and Zhao, 2012), and teleseismic Vp (Searcy *et al*., 1996; Qi *et al*., 2007). Pre-ATA large-scale surface-wave studies were carried out by Wang and Tape (2014) and Ward (2015). Since the ATA deployment, a sizable number of studies using surface waves for tomography have been published, using ambient noise cross-correlation (ANCC) and earthquakes (Feng and Ritzwoller, 2019), ANCC data and teleseismic S waves (Jiang *et al*., 2018), ANCC data and receiver functions (Ward and Lin, 2018) or ANCC and earthquake surface waves and receiver functions (Martin-Short *et al*., 2018; Berg *et al*., 2020). Receiver functions (Miller *et al*., 2018; Miller and Moresi, 2018) and body-wave arrival times from local and teleseismic earthquakes (Martin-Short *et al*., 2016; Allam *et al*., 2017; Gou *et al*., 2019; Gou *et al*., 2020) have also been used for imaging.

In this study, we take advantage of a combination of regional body-wave data and surface-wave data from ambient noise in a joint inversion for Vp and Vs or Vp and Vp/Vs, using two different joint inversion methods. Our goal is the development of 3D velocity models that would be useful for obtaining more accurate earthquake locations as well as for computing wavefield simulations for hypothetical future large earthquakes in Alaska. First we describe the data set and the two inversion methods, then we present the results from the two methods and some comparisons of the two models and an earlier model. The main model features are generally quite similar among all three models, but due to the inclusion of surface-wave data, resolution of the upper crust is substantially improved in the two new models.

Model Domain and Dataset

The starting point for our tomography work is the study of Eberhart-Phillips *et al.* (2006) on development and interpretation of a 3-D model of the Vp and Vp/Vs structure of south-central Alaska. That study covered a region 1,000 km NNE-SSW by 700 km WNW-ESE centered on Anchorage, and included data from 1,752 earthquakes with about 64,000 first-P arrivals and nearly 20,000 S-P times, plus close to 15,000 first-P arrivals from explosions and marine air gun shots. It was the first tomographic study in Alaska to include data from both active sources and from the first broadband experiment (BEAAR: Ferris *et al.* 2003).

We have developed our new models in two steps. First, we expanded the model domain to cover more of south-central Alaska, assembling body-wave and surface-wave data to cover the enlarged model region. In the second step, we further extended the model domain to encompass almost the entire state and a small part of northwestern Canada, the part covered by the ATA. The two joint inversion codes represent the model domain differently, one with a Cartesian system (and an earth-flattening transformation), the other in spherical geographic coordinates. The former covers a region 1,900 km NNE-SSA by 1,600 km ENE-WSW, again centered on Anchorage (Model AKEP2020), and the latter covers a region extending 46.4° in longitude and 21.2° in latitude centered on 61.5° North, 150° West (Model AKAN2020). A map of the station distribution is shown in Figure 1a.

The body-wave data were obtained from multiple sources. The vast majority of the new P-wave arrival times are from the AEC earthquake catalog. Arrival times were also generously provided to us from the BEAAR and MOOS datasets (Ferris *et al.*, 2003; Li *et al.*, 2013). Many additional P-wave arrivals and the majority of the S-wave arrivals from these and other temporary station datasets were obtained using a modified version of the iterative autopicking software package called REST (Lanza *et al.*, 2019). The additional datasets we tapped for more body-wave data included SALMON (Tape *et al.*, 2017), FLATS (Tape *et al.*, 2018), and the on-shore part of the Alaska Amphibious Community Seismic Experiment, AACSE (Abers *et al.*, 2019). A map of the earthquake and shot distribution is shown in Figure 1b. A complete list of networks used in this study is provided in the Data and Resources section.

The surface-wave data we use come entirely from ambient noise. We carried out multi-component ANCC. An improvement over other rigorous ambient noise derived surface-wave tomography studies (Feng and Ritzwoller, 2019; Berg *et al.*, 2020) is the inclusion of short-period stations and recently deployed temporary and permanent broadband stations (see Data and Resources). In particular, using stations from the AV, XO and CN networks significantly improved coverage in the Aleutian arc, the area between Katmai peninsula and Kodiak island, and the south-eastern end of Alaska, respectively. We used standard methods (see references in Nayak and Thurber (2020)) and preserve the relative amplitudes among the three components of motion (Lin *et al.*, 2014) that allows us to rotate the cross-correlation tensors from the East-North-Vertical (E-N-Z) to the Transverse-Radial-Vertical (T-R-Z) reference frame. The four components in the radial-vertical plane (RR, RZ, ZR, and ZZ) were stacked with appropriate phase shifts to extract improved Rayleigh-wave dispersion measurements (Nayak and Thurber, 2020). The TT component was used to measure Love-wave dispersion. We applied automatic frequency-time analysis (AFTAN) methodology (Bensen *et al.*, 2007; Lin *et al.*, 2008) to the noise cross-correlations to extract the dispersion measurements. We also verified the approximate orientation and polarity information of all three-component stations in our study (Nayak and Thurber, 2020). We found errors in metadata for a few stations archived at IRIS that might have led to incorrect phase velocity measurements in previous studies. We started with group velocity dispersion measurements using a 1-D model as a reference. The reference 1-D model is a weighted average of the three 1-D velocity models used by the AEC for moment tensor inversion of earthquakes in different regions of Alaska.

We inverted Rayleigh-wave (periods $\sim$5.2 s to $\sim$35 s) and Love-wave (periods $\sim$7.1 s to $\sim$35 s) group velocity dispersion measurements to determine state-wide group velocity maps at each period with a grid spacing of 0.4° in latitude and 0.8° in longitude ($\sim$40 km), using the 2-D fast marching surface-wave tomography method (Rawlinson and Sambridge, 2004). Dispersion measurements in this period range are primarily sensitive to depths down to $\sim$70 km. For each latitude-longitude point in the maps, we jointly inverted the Rayleigh-wave and Love-wave group velocity dispersion for a vertical Vs profile using the surf96 algorithm (Herrmann, 2013). In this study, we neglect possible anisotropy (Feng and Ritzwoller, 2019) and invert for isotropic velocities only. We found the greatest inconsistency between short period Rayleigh and Love wave measurements in the Colville Basin, consistent with the observations of Feng and Ritzwoller (2019). Further details on parameterization of the model and the inversion are provided in the electronic supplement. Group velocity at each period at each node was weighted by the Derivative Weight Sum (DWS) (Thurber and Eberhart-Phillips, 1999) at that node in the group velocity map at that particular period. Vp was scaled to Vs using Brocher (2005) relations in the inversion, as surface-wave dispersion has negligible sensitivity to Vp at these periods. Thereafter, we assembled a 3-D Vs model from the resulting set of 1-D models.

In the next step, the 3-D velocity model was used as a reference model to measure Rayleigh-wave and Love-wave phase velocity dispersion using AFTAN. Phase velocities are more precisely measured and more consistent with the eikonal-equation-based fast marching tomography method compared to group velocities. The Rayleigh-wave and Love-wave phase velocity measurements were inverted for 2-D phase velocity maps. Direct inversion of phase travel times using the fast marching method is possibly an improvement over eikonal tomography methods (Berg *et al*., 2020) that allow ray bending but involve fitting of phase arrival times to smoothed maps. This procedure of re-picking dispersion measurements, inverting for phase velocity maps, and inverting for a 3-D Vs model was repeated one more time for full consistency. For Rayleigh waves at each period, the number of dispersion measurements ranged from ∼26,000 to ∼90,000, and the number of stations was ∼790. For Love waves, the corresponding numbers were ∼23,000 to ∼64,000 and ∼680. Phase velocity maps and the ray coverage for two of the better constrained periods are shown in Figure 2. Inclusion of shorter-period Rayleigh-wave phase velocity measurements (∼5-8 s) than in previous studies helps to constrain shallower velocity structure in the absence of Rayleigh-wave ellipticity measurements in the inversion (Berg *et al*., 2020). Example phase velocity maps masked by DWS and DWS maps for a number of periods are shown in the electronic supplement Figure S1. The surface-wave results were used in two different ways, as described in the next section.

Tomographic Inversion Methods

Joint inversion with the Eberhart-Phillips and Fry (2017) algorithm

Tomographic inversion for hypocenters and 3-D Vp and Vp/Vs structure was done with a gradational approach, using arrival-time observations from the AK2006 study (Eberhart-Phillips *et al*., 2006), adding recent body-wave data, and incorporating group velocity maps, as described above. For typical earthquake arrival-time datasets, if the inversion is done to obtain Vp and Vs, it is generally the case that the Vs model is poorly constrained relative to the Vp model, less representative of crustal structure, and difficult to use for interpreting Vp/Vs (Eberhart-Phillips, 1990). Thus, as described by Eberhart-Phillips and Reyners (1997), it is preferable to solve for Vp and Vp/Vs when using local earthquake arrival-time data. This parameterization is retained for the group velocity data, with the Herrmann (2013) Vp kernels related to Vp model inversion parameters and

Vs kernels related to partial derivatives of Vp and Vp/Vs model parameters (Eberhart-Phillips and Fry, 2017). Model Cartesian coordinates and distances are computed with Transverse Mercator conversion, and an earth-flattening transformation is used. The 0 km model depth is at sea level, travel-time ray-tracing includes station elevations, and elevation for group velocity observations is from the 30 km median topography.

Eberhart-Phillips and Fry (2017) explicitly consider the frequency-dependent spatial sensitivity of surface waves both in depth and laterally. As illustrated in Figure 3a, in the volume surrounding each group velocity observation, numerous points are used for relating the group velocity observation to the gridded 3-D tomography model, analogous to points along a ray path. The partial derivatives at the points are computed using the group velocity sensitivity kernels for Vp and Vs.

A gradational approach is used for velocity inversions. This provides reasonable velocities throughout the region, and more detail where there is denser data coverage. The initial model used a coarse version of the Eberhart-Phillips *et al.* (2006) model, with some extrapolation down the Alaska Peninsula, and very coarse models with recent data for distant areas. An inversion of the whole model area was done with ~50 km grid spacing. Then fine inversions were done with ~25 km grid spacing and auto-linking in low resolution areas (Eberhart-Phillips *et al.*, 2014) for the final body-wave model. This model was used as the initial model for the joint inversions.

A progressive series of joint inversions was done to promote improvement of the shallowest depths, with the deepest portions of the model fixed. The relative weight of the group velocity observations (wtU) is varied. This series comprised (a) 1 iteration for depth $z = -1$ km free and wtU=35; (b) 2 iterations for $z = -1$, 2 km free and wtU=22; (c) 1 iteration for $z = -1$, 2, 6 km free and wtU=10; and (d) 2 iterations for $z = -1$ through 33 km free and wtU=5.5. The final model achieves good improvement in fitting the expanded data set. Compared to the initial model, the final model AKEP2020 provides 36.4% decrease in P data variance, 24.6% decrease in S-P data variance, and 96.7% decrease in group velocity data variance.

Joint inversion with the Fang et al. (2016) algorithm

As discussed in the Model Domain and Dataset section, we carried out a multi-step process with the ambient noise surface-wave data, resulting in Rayleigh- and Love-wave group and phase velocity measurements and the corresponding group and phase velocity maps at a range of frequencies. As noted above, a 3-D Vs model was derived from the Rayleigh- and Love-wave phase velocity measurements by stitching together the results of 1-D inversions at each model grid point. We also carried out a separate body-wave tomography analysis in order to get an initial model for the joint inversion. We used a larger body-wave dataset containing $\sim$890,000 P-wave picks and $\sim$270,000 S-wave picks from $\sim$5,800 earthquakes and the explosion dataset of Eberhart-Phillips *et al.* (2006). For all earthquakes, P-wave and S-wave picks were limited to epicentral distances of $\sim$900 km and $\sim$600 km, respectively. Additionally, in order to prevent errors in S-wave picks from misidentifying Sg as first arriving Sn at post-critical distances, we limited S-wave picks to $\sim$250 km epicentral distance for crustal earthquakes (depth $\leq$ 45 km). As earthquakes occur primarily in the crust and only TA stations are present at spacing $\sim$70-80 km in northern half of Alaska, our constraints on Vs from body-wave data in northern half of Alaska are weaker and our Vs sensitivity is limited to the crust. We used a spherical earth version of tomoDD (Zhang *et al.*, 2004) with ray tracing in spherical coordinates to invert for a state-wide body-wave velocity model of Alaska with the same grid spacing of 0.8° in longitude and 0.4° in latitude (approximately $\sim$40 km) as for the surface-wave modeling. However, the region for our body-wave tomography was slightly smaller than that for surface-wave tomography. More earthquake data from the western Aleutian volcanic arc were added later during the joint inversion to invert for the slightly larger model. We tested 375 different combinations of damping and smoothing parameters to check the trade-off between final misfit and model complexity. For the optimum combination of smoothing and damping parameters, the weighed misfit decreased from $\sim$1.5 s for an initial 1-D model to $\sim$0.43 s for the final 3-D model. The body-wave travel-times provide sensitivity down to a depth of $\sim$150 km around the subduction zone. The body-wave tomography results and resolution indicated by scaled DWS values are shown in electronic supplement Figure S2. The DWS values of Vp and Vs from the body-wave tomography model were scaled from ∼100 to 10,000 to weights ∼0 to 1. These weights were used to merge the final body-wave model with the final surface-wave model to assemble an initial model for the joint inversion.

The Fang *et al*. (2016) joint inversion method utilizes a direct inversion approach (Fang *et al*., 2015) for relating surface-wave dispersion data to the 3-D Vs and Vp models, in contrast to the more common two-step approach used by many researchers. The method represents the 3-D Vs model by means of 1-D profiles beneath grid points (Figure 3b), and those 1-D profiles are determined from all dispersion data simultaneously. An equality constraint on Vp/Vs (∼1.75) is used to facilitate combined improvement of both Vp and Vs, with a damping parameter to regulate the strength of this constraint (Fang *et al*., 2016). We made considerable improvements to the original Fang et al. (2016) inversion software: (1) introducing latitude-dependent smoothing in longitude that accounts for the large change in length of a degree of longitude across the north-south extent of our model, (2) introducing signal-to-noise-ratio (SNR) dependent weights for surface-wave phase travel times on the scale of ∼0.5 to 1, (3) automatic recalculation of relative weights between body-wave data and surface-wave data based on the misfits at each iteration and (4) general improvements in the efficiency of the software that made it possible to use it for a large dataset (∼1 million earthquake body-wave travel times and ∼1.7 million surface-wave phase travel times). The SNR values of surface-wave dispersion measurements (∼2-8 scaled to ∼0.5-1.0) generally decrease with interstation distance and are highest for the primary and secondary microseism passbands.

To start the joint inversion of body-wave and surface-wave datasets using the Fang *et al*. (2016) algorithm, we used the same earthquake data from the body-wave tomography. Rayleigh- and Love-wave phase velocity dispersion measurements were selected at 17 and 15 periods, respectively, and we used the same grid spacing of 0.4° in latitude and 0.8° in longitude (∼40 km) as for the surface-wave phase velocity map inversions. It is possible that smaller scale features are resolvable in south-central Alaska where the stations are relatively dense, but a lower grid spacing was not attempted for computational reasons. Station elevations were used for body-wave data but an elevation of -1 km was assumed as reference depth = 0 km for surface-wave data with no corrections applied for topography. We tested two initial models, the final model from surface-wave tomography and a weighted average of final models from body-wave and surface-wave tomography. To construct the weighted average model, Vp and Vs from the body-wave model were used along with the corresponding weights calculated from the scaled DWS values, with the weights further doubled for Vp, which is significantly better constrained by body-wave data than by surface-wave data. The model from surface-wave tomography was assigned laterally uniform weight at 1.0 and progressively smaller weights below a depth of $\sim$100 km. Vp was scaled to Vs using Brocher (2005) relations. Vp/Vs ratio for the initial model was restricted to the range of $\sim$1.55 to $\sim$2.6; the high Vp/Vs ratio $\geq$2.0 primarily results from the Brocher (2005) relations applied to low Vs values in the sedimentary basins. In the course of the inversion, the Vp/Vs ratio was progressively perturbed towards a value of $\sim$1.75 in regions where high or low values are not supported by the data. The final model, AKAN2020, was obtained using the averaged body-wave and surface-wave model as the initial model. The final weighted misfit for the body-wave and surface-wave datasets were $\sim$0.4 s and $\sim$1.5 s, respectively, very close to the final misfit for the separate inversions of the two datasets.

Comparisons of tomographic models

Direct comparison of the AKEP2020 model to the AKAN2020 model, and the comparison of both to the AKEP2006 model, is limited because for AKEP2020 and AKEP2006, the inversion solves for Vp and Vp/Vs, whereas for AKAN2020, the inversion solves for Vp and Vs. It is widely recognized that a Vp/Vs model obtained by dividing Vp by Vs is prone to substantial artifacts (Eberhart-Phillips, 1990; Thurber and Ritsema, 2015; Watkins *et al*., 2018). This is due mainly to the normally inferior resolution for Vs, leading to apparent Vp/Vs variations in the model where

Vp is well resolved and has perturbations but Vs is poorly resolved and therefore has at most minor perturbations. On the other hand, it has been our experience that obtaining Vs by dividing Vp by Vp/Vs appears to be more stable (Watkins *et al*., 2018), so here we compare the directly inverted Vp models and both the directly inverted and division-derived Vs models. Comparisons of Vp/Vs results for the two directly-determined models, AKEP2006 and AKEP2020, are also presented.

Large-scale deep structure

To first order, the large-scale and deeper parts of the three Vp models are quite similar. This is because the earthquakes in the previous and new body-wave datasets have similar spatial distributions, although the station distribution is notably improved for the new model thanks to a number of temporary array deployments, including the ATA.

In Figure 4, we compare map-view slices through the three models, AKEP2006, AKEP2020, and AKAN2020, at a depth of 57 km as representative of the deeper structure. Despite the differences in datasets and geographic coverage, the main features in the area of overlap are reasonably consistent. The subducting Pacific Plate is evident offshore and beneath Kodiak Island and Kenai Peninsula. Lower velocities in the mantle wedge are prevalent, extending all the way north to the Denali fault.

Figures 5 and 6 show representative Vp, Vs, and Vp/Vs cross-sections through the three models on a profile normal to the Denali fault. The AKEP2020 and AKEP2006 models are the most similar, with AKAN2020 showing lower velocities in the lower part of the slab for both Vp and Vs. We attribute this to a greater contribution of the surface-wave data relative to the body-wave data in the AKAN2020 inversion, since both Love and Rayleigh wave phase velocity data are included. We also note that the Hayes *et al*. (2018) slab surface appears to be too shallow along this cross-section, a trend we observe in many cross-sections through the subducting slab.

Shallow basin structures

Figure 7 shows cross-sections through Cook Inlet for the three models. The apparent basin thickness is quite different in all three models. We suspect that the deep low velocities in the AKEP2020 model are an overestimate of the actual depth extent. In contrast, the AKAN2020 model appears to overestimate the width of the basin structure, presumably due to smearing caused by the surface-wave data and coarser grid spacing (40 km versus 25 km for AKEP2006 and AKEP2020 in this region). A view zooming in on the shallow Vs is shown in Figure S3. The pattern is similar for cross-sections through the Copper River Basin, as shown in Figure 8. The basin depth appears substantially greater in model AKEP2020, and the width is again much greater for model AKAN2020.

Statewide Velocity Model

Model AKAN2020 provides new constraints on the seismic velocity structure in Alaska compared to previously published studies; some features are briefly described here. Figures 9, S4, and S5 show depth slices from AKAN2020 for a range of depths.

Inclusion of ambient noise derived surface-wave phase velocities from a large number of stations not used in previous studies allows us to loosely constrain Vs in offshore areas. These include AV short-period stations in the Aleutian volcanic arc, AK/TA stations on St. George, St. Paul and St. Lawrence Islands and CN stations on Haida Gwaii Archipelago. However, the resolution is low because most of the interstation paths have similar azimuths and there are no constraints on Vp in offshore areas because no body-wave data are available. Paths between the Aleutian Arc and southeastern Alaska traversing the Gulf of Alaska provide constraints on the offshore section of the subducting Pacific plate (Figure S1c,d). These longer period measurements ($\geq$ 14 s) reveal higher velocities in the subducting oceanic mantle of the Pacific plate in the offshore region of the subduction zone at depths $\geq$15 km (Figure S5c-f). Similarly, we are able to image the approximate outline of the North Aleutian/Bristol Bay Basin in the Bering Sea, north of the Aleutian arc

(Kirschner, 1988) (Figure S1b,c and Figure 9a). We observe general NW-SE widening of the basin delineated by low values of Vs consistent with Kirschner (1988). We are also weakly sensitive to the Norton Basin to the southwest of Seward Peninsula (Figure S1b,c and Figure 9a).

We are able to recover low seismic velocities consistent with most inland sedimentary basins observed in previous studies (Feng and Ritzwoller, 2019; Berg *et al.*, 2020), with noticeable improvement in the outline of the basins in the top $\sim$1 km (Figure 9a). Despite coarse grid spacing, we are even sensitive to smaller basins such as the Susitna Basin north of Cook Inlet. Similar to Berg *et al.* (2020), we assume the depth to Vs $\sim$3.1 km/s to be the basement depth and estimate the maximum depths of the major basins. Our estimates of Vs at the reference depth and basin depths are: Cook Inlet, $\sim$1.0-1.2 km/s, $\sim$7-10 km; Nenana, $\sim$1.2-1.3 km/s, $\sim$4-6 km; Copper River and Bethel, $\sim$1.7-1.8 km/s, $\sim$5-6 km; North Aleutian/Bristol Bay, $\sim$1.3-1.4 km/s, $\sim$7-10 km; Norton, $\sim$1.0-1.2 km/s, $\sim$3-5 km; Yukon Flats, $\sim$1.3-1.4 km/s, $\sim$4-5 km; Gulf of Alaska, $\sim$1.7-1.8 km/s, $\sim$11-15 km; and Colville Basin, $\sim$1.3-1.4 km/s, $\sim$10-11 km. The very shallow velocities (depth $\leq$ 1 km) in offshore areas and the northern region of Alaska (such as in Colville Basin) are likely to be an upper bound because shorter-period measurements are not available due to the coarser station spacing. Two inconsistent features are a region of low velocities north of Yukon Flats Basin that is not present in previous models and no recovery of low velocities corresponding to Selawik Trough (Berg *et al.*, 2020). Among the basins, constraint on Vp from body-wave data is strongest in the northern section of the Cook Inlet Basin (Figure S2a).

The Denali fault is one of the most prominent tectonic features in Alaska. We see a sharp contrast in Vp across the Denali fault between the Yukon composite terrane (faster) and Wrangellia composite terrane (slower) in the upper mantle wedge between the depths of $\sim$25 km to $\sim$50 km (Figure 9b) for a significant distance along the fault, similar to that observed in previous studies, but not as clearly (Eberhart-Phillips *et al.*, 2006; Allam *et al.*, 2017; Martin-Short *et al.*, 2018; Feng and Ritzwoller, 2019; Berg *et al.*, 2020). The mantle wedge appears to extend to the Aleutian arc, west of the Kodiak island. We also see a strong velocity contrast across the Eastern Denali fault at the southeastern end of Alaska at shallow depths ($\leq$ 3 km) that has not been observed in previous studies. We are also able to detect low velocity sediments in the Hecate Strait off the coast of British Columbia. Berg *et al.* (2020) observed low Vs in the lower crust under Brooks Range related to fold-and-thrust crustal thickening. Using constraints provided by body-wave arrivals times from crustal earthquakes, we see similar low values of Vp under the Brooks Range (Figures S2 and 9b), a feature not clearly present in the body-wave tomography results of Gou *et al.* (2019).

Discussion and Conclusions

We can use independent information to assess the accuracy of some aspects of these models. For example, Shellenbaum *et al.* (2010) present a map of the depth to basement beneath the Cook Inlet basin, based on a combination of marine seismic reflection data and oil and gas wells that penetrated the basement. The maximum basement depth from their map is about 7.5 km. If we adopt Vp $\sim$4.7 km/s as representing basement (Lutter *et al.*, 2004), then the AKEP2020 and AKEP2006 models substantially overestimate basin depth, by about 50%. In contrast, model AKAN2020 shows very good agreement with Shellenbaum *et al.* (2010). According to Fuis *et al.* (1991), maximum basement depth in the Copper River Basin is approximately 5 km, based on seismic refraction data. In this case, all three models are generally consistent with this basement depth value, again assuming that Vp $\sim$4.7 km/s represents basement.

Validating the deeper structure of these models is not straightforward. We find that the depth to the top of the slab, based on the seismicity distribution, is greater than that of Hayes *et al.* (2018) virtually everywhere in our models. This presumably reflects the fact that our earthquake locations are determined in a 3-D model rather than a 1-D model. Validating the earthquake depths and/or validating the deeper structure will require wavefield simulations. Since the AKEP2020 and AKAN2020 models incorporate surface-wave data, we can expect that those models will perform better in a comparison between simulated waveforms and observations from actual earthquakes.

Data and Resources

All seismic data data at Global Seismic Network stations are freely available at the IRIS DMC. The majority of the data are from the following seismic networks: AK (Alaska Earthquake Center, Univ. of Alaska Fairbanks, 1987), AV (Alaska Volcano Observatory/USGS, 1988), CN (Geological Survey of Canada, 1989), AT (NOAA, 1967), TA (IRIS, 2003), XE (Christensen *et al.*, 1999), ZE (Tape *et al.*, 2015) and XO, the onshore component of the AACSE network. Data from additional networks are indicated in the electronic supplement. Models AKEP2020 and AKAN2020 are available from the IRIS Earth Model Collaboration (`http://ds.iris.edu/ds/products/emc/`). The facilities of IRIS Data Services, and specifically the IRIS Data Management Center, were used for access to waveforms, related metadata, and/or derived products used in this study. IRIS Data Services are funded through the Seismological Facilities for the Advancement of Geoscience (SAGE) Award of the National Science Foundation under Cooperative Support Agreement EAR-1851048. The supplemental material includes example surface-wave phase velocity maps at a range of periods, coverage, depth slices from the body-wave tomography model and coverage, a cross-section through the Cook Inlet basin and example depth slices for the AKAN2020 model.

Acknowledgments

This material is based upon work supported by the U.S. Geological Survey under Grant Nos. G18AP00017 and G19AP00019. M.M.M, C.T., and D.H.C. were supported by National Science Foundation Grant EAR 1251971. A.N. thanks Robert Herrmann (St. Louis Univ.) for helpful discussions about surface waves.

References

Abers, G. A., A. N. Adams, P. J. Haeussler, E. Roland, P. J. Shore, D. A. Wiens, S. Y. Schwartz, A. F. Sheehan, D. J. Shillington, S. Webb, and L. L. Worthington (2019). Examining Alaska's Earthquakes on Land and Sea. *EOS 100*, doi: 10.1029/2019EO117621.

Alaska Earthquake Center, Univ. of Alaska Fairbanks (1987). Alaska Regional Network. International Federation of Digital Seismograph Networks. Other/Seismic Network. `doi:10.7914/SN/AK`.

Alaska Volcano Observatory/USGS (1988). Alaska Volcano Observatory. International Federation of Digital Seismograph Networks. Other/Seismic Network. `doi:10.7914/SN/AV`.

Allam, A. A., V. Schulte-Pelkum, Y. Ben-Zion, C. Tape, N. Ruppert, and Z. E. Ross (2017). Ten kilometer vertical Moho offset and shallow velocity contrast along the Denali fault zone from double-difference tomography, receiver functions, and fault zone head waves. *Tectonophysics 721*, 56–69, doi: 10.1016/j.tecto.2017.09.003.

Bensen, G. D., M. H. Ritzwoller, and N. M. Shapiro (2007). Broadband ambient noise surface wave tomography across the United States. *J. Geophys. Res. 113*, 1–21, doi: 10.1029/2007JB005248.

Berg, E. M., F.-C. Lin, A. Allam, V. Schulte-Pelkum, K. M. Ward, and W. Shen (2020). Shear velocity model of Alaska via joint inversion of Rayleigh wave ellipticity, phase velocities, and receiver functions across the Alaska transportable Array. *J. Geophys. Res. Solid Earth 125*, doi: 10.1029/2019JB018582.

Brocher, T. M. (2005). Empirical relations between elastic wavespeeds and density in the Earth's crust. *Bull. Seismol. Soc. Am. 95*(6), 2081–2092.

Christensen, D., G. Abers, and R. Hansen (1999). Broadband Experiment Across the Alaska Range. International Federation of Digital Seismograph Networks. Other/Seismic Network. `10.7914/SN/XE_1999`.

Eberhart-Phillips, D. (1990). Three-dimensional *P* and *S* velocity structure in the Coalinga region, California. *J. Geophys. Res. 95*(B10), 15,343–15,363.

Eberhart-Phillips, D., S. Bannister, and S. Ellis (2014). Imaging *P* and *S* attenuation in the termination region of the Hikurangi subduction zone, New Zealand. *Geophys. J. Int. 198*, 516–536, doi: 10.1093/gji/ggu151.

Eberhart-Phillips, D., D. H. Christensen, T. M. Brocher, R. Hansen, N. A. Ruppert, P. J. Haeussler, and G. A. Abers (2006). Imaging the transition from Aleutian subduction to Yakutat collision in central Alaska, with local earthquakes and active source data. *J. Geophys. Res. 111*, doi: 10.1029/2005JB004240.

Eberhart-Phillips, D. and B. Fry (2017). A new scheme for joint surface wave and earthquake travel-time inversion and resulting 3-D velocity model for the western North Island, New Zealand. *Phys. Earth Planet. Inter. 269*, 98–111, doi: 10.1016/j.pepi.2017.05.014.

Eberhart-Phillips, D. and M. Reyners (1997). Continental subduction and three-dimensional crustal structure: The northern South Island, New Zealand. *J. Geophys. Res. 102*(B6), 11,843–11,861.

Fang, H., H. Yao, H. Zhang, Y.-C. Huang, and R. D. van der Hilst (2015). Direct inversion of surface wave dispersion for three-dimensional shallow crustal structure based on ray tracing: methodology and application. *Geophys. J. Int. 201*, 1251–1263, doi: 10.1093/gji/ggv080.

Fang, H., H. Zhang, H. Yao, A. Allam, D. Zigone, Y. Ben-Zion, C. Thurber, and R. D. van der Hilst (2016). A new algorithm for three-dimensional joint inversion of body wave and surface wave data and its application to the Southern California plate boundary region. *J. Geophys. Res. Solid Earth 121*, 3557–3569, doi: 10.1002/2015JB012702.

Feng, L. and M. H. Ritzwoller (2019). A 3-D shear velocity model of the crust and uppermost mantle beneath Alaska including apparent radial anisotropy. *J. Geophys. Res. Solid Earth 124*, 10,468–10,497, doi: 10.1029/2019JB018122.

Ferris, A., G. A. Abers, D. H. Christensen, and E. Veenstra (2003). High resolution image of the subducted Pacific (?) plate beneath central Alaska, 50–150 km depth. *Earth Planet. Sci. Lett. 214*, 575–588.

Fuis, G. S., E. L. Ambos, W. D. Mooney, N. I. Christensen, and E. Geist (1991). Crustal structure of accreted terranes in southern Alaska, Chugach Mountains and Copper River basin, from seismic refraction results. *J. Geophys. Res. 96*(B3), 4187–4227.

Geological Survey of Canada (1989). Canadian National Seismograph Network. International Federation of Digital Seismograph Networks. Other/Seismic Network. doi:10.7914/SN/CN.

Gou, T., D. Zhao, Z. Huang, and L. Wang (2019). Aseismic deep slab and mantle flow beneath Alaska: Insight from anisotropic tomography. *J. Geophys. Res. Solid Earth 124*, 1700–1724, doi: 10.1029/2018JB016639.

Gou, T., D. Zhao, Z. Huang, and L. Wang (2020). Structural heterogeneity in source zones of the 2018 Anchorage intraslab earthquake and the 1964 Alaska megathrust earthquake. *Geochem. Geophy. Geosyst. 21*, doi: 10.1029/2019GC008812.

Hayes, G. P., G. L. Moore, D. E. Portner, M. Hearne, H. Flamme, M. Furtney, and G. M. Smoczyk (2018). Slab2, a comprehensive subduction zone geometry model. *Science 362*, 58–61, doi: 10.1126/science.aat4723.

Herrmann, R. B. (2013). Computer programs in seismology: An evolving tool for instruction and research. *Seismol. Res. Lett. 84*(6), 1081–1088, doi: 10.1785/0220110096.

IRIS (2003). USArray Transportable Array. International Federation of Digital Seismograph Networks. Other/Seismic Network. doi:10.7914/SN/TA.

Jiang, C., B. Schmandt, K. M. Ward, F.-C. Lin, and L. L. Worthington (2018). Upper mantle seismic structure of Alaska from Rayleigh and *S* wave tomography. *Geophys. Res. Lett. 45*, 10,350–10,359, doi: 10.1029/2018GL079406.

Kirschner, C. E. (1988). Map Showing Sedimentary Basins of Onshore and Continental Shelf Areas, Alaska. U.S. Geol. Survey Miscellaneous Investigation Series I-1873.

Kissling, E. and J. C. Lahr (1991). Tomographic image of the Pacific Slab under southern Alaska. *Eclogae geol. Helv. 84*(2), 297–315.

Lanza, F., C. J. Chamberlain, K. Jacobs, E. Warren-Smith, H. J. Godfrey, M. Kortink, C. H. Thurber, M. K. Savage, J. Townend, S. Roecker, and D. Eberhat-Phillips (2019). Crustal fault connectivity of the M_w 7.8 2016 Kaikōura earthquake constrained by aftershock relocations. *Geophys. Res. Lett. 46*, 6487–6496, doi: 10.1029/2019GL082780.

Li, J., G. A. Abers, Y. Kim, and D. Christensen (2013). Alaska megathrust 1: Seismicity 43 years after the great 1964 Alaska megathrust earthquake. *J. Geophys. Res. 118*, 4861–4871, doi: 10.1002/jgrb.50358.

Lin, F.-C., M. P. Moschetti, and M. H. Ritzwoller (2008). Surface wave tomography of the western United States from ambient seismic noise: Rayleigh and Love wave phase velocity maps. *Geophys. J. Int. 173*, 281–298.

Lin, F.-C., V. C. Tsai, and B. Schmandt (2014). 3-D crustal structure of the western United States: application of Rayleigh-wave ellipticity extracted from noise cross-correlations. *Geophys. J. Int. 198*, 656–670.

Lutter, W. J., G. S. Fuis, T. Ryberg, D. A. Okaya, R. W. Clayton, P. M. Davis, C. Prodehl, J. M. Murphy, V. E. Langenheim, M. L. Benthien, N. J. Godfrey, N. I. Christensen, K. Thygesen, C. H. Thurber, G. Simila, and G. R. Keller (2004). Upper crustal structure from the Santa Monica Mountains to the Sierra Nevada, southern California: Tomographic results from the Los Angeles Regional Seismic Experiment, Phase II (LARSE II). *Bull. Seismol. Soc. Am. 64*(2), 619–632.

Martin-Short, R., R. Allen, I. D. Marstow, R. W. Porritt, and M. S. Miller (2018). Seismic imaging of the Alaska subduction zone: Implications for Slab Geometry and Volcanism. *Geochem. Geophy. Geosyst. 19*, 4541–4560, doi: 10.1029/2018GC007962.

Martin-Short, R., R. M. Allen, and I. D. Barstow (2016). Subduction geometry beneath south central Alaska and its relationship to volcanism. *Geophys. Res. Lett. 43*, 9509–9517, doi: 10.1002/2016GL070580.

Miller, M. S. and L. Moresi (2018). Mapping the Alaska Moho. *Seismol. Res. Lett. 89*(6), 2430–

2436, doi: 10.1785/0220180222.

Miller, M. S., L. J. O'Driscoll, R. W. Porritt, and S. M. Roeske (2018). Multiscale crustal architecture of Alaska inferred from P receiver functions. *Lithosphere 10*(2), 267–278, doi: 10.1130/L701.1.

Nayak, A. and C. H. Thurber (2020). Using multi-component ambient seismic noise cross-correlations to identify higher mode Rayleigh waves and improve dispersion measurements. *Geophys. J. Int.*, doi: 10.1093/gji/ggaa270.

NOAA (1967). National Tsunami Warning Center Alaska Seismic Network. International Federation of Digital Seismograph Networks. Other/Seismic Network. `doi:10.7914/SN/AT`.

Qi, C., D. Zhao, and Y. Chen (2007). Search for deep slab segments under Alaska. *Phys. Earth Planet. Inter. 165*, 68–82.

Qi, C., D. Zhao, Y. Chen, and N. A. Ruppert (2007). New insight into the crust and upper mantle structure under Alaska. *Polar Science 1*, 85–100.

Rawlinson, N. and M. Sambridge (2004). Wave front evolution in strongly heterogeneous layered media using the fast marching method. *Geophys. J. Int. 156*, 631–647, doi: 10.1111/j.1365-246X.2004.02153.x.

Searcy, C. K., D. H. Christensen, and G. Zandt (1996). Velocity structure beneath College station Alaska from receiver functions. *Bull. Seismol. Soc. Am. 86*(1A), 232–241.

Shellenbaum, D. P., L. S. Gregersen, and P. R. Delaney (2010). Top Mesozoic unconformity depth map of the Cook Inlet Basin, Alaska. doi: 10.14509/21961. Alaska Div. Geol. Geophys. Surv. Report of Investigation 2010-2, 1 sheet, scale 1:500,000, available at `http://www.dggs.alaska.gov/pubs/id/21961` (last accessed 2016-10-30).

Tape, C., D. Christensen, M. M. Moore-Driskell, J. Sweet, and K. Smith (2017). Southern Alaska Lithosphere and Mantle Observation Network (SALMON): a seismic experiment covering the active arc by road, boat, plane, and helicopter. *Seismol. Res. Lett. 88*(4), 1185–1202, doi:

10.1785/0220160229.

Tape, C., D. H. Christensen, and M. M. Driskell (2015). Southern Alaska Lithosphere and Mantle Observation Network. International Federation of Digital Seismograph Networks. Other/Seismic Network. doi:10.7914/SN/ZE_2015.

Tape, C., S. Holtkamp, V. Silwal, J. Hawthorne, Y. Kaneko, J. P. Ampuero, C. Ji, N. Ruppert, K. Smith, and M. E. West (2018). Earthquake nucleation and fault slip complexity in the lower crust of central Alaska. *Nature Geoscience 11*, 536–541, doi: 10.1038/s41561-018-0144-2.

Thurber, C. and D. Eberhart-Phillips (1999). Local earthquake tomography with flexible gridding. *Computers & Geosciences 25*, 809–818.

Thurber, C. and J. Ritsema (2015). Seismic tomography and inverse methods. In G. Schubert (Ed.), *Seismology and Structure of the Earth* (2 ed.), Volume 1 of *Treatise on Geophysics*, pp. 307–337. Elsevier.

Tian, Y. and D. Zhao (2012). Seismic anisotropy and heterogeneity in the Alaska subduction zone. *Geophys. J. Int. 190*, 629–649, doi: 10.1111/j.1365-246X.2012.05512.x.

van Stiphout, T., E. Kissling, S. Wiemer, and N. Ruppert (2009). Magmatic processes in the Alaska subduction zone by combined 3-D b value imaging and targeted seismic tomography. *J. Geophys. Res. 114*, 1–16, doi: 10.1029/2008JB005958.

Wang, Y. and C. Tape (2014). Seismic velocity structure and anisotropy of the Alaska subduction zone derived from surface wave tomography. *J. Geophys. Res. Solid Earth 119*, 8845–8865, doi: 10.1002/2014JB011438.

Ward, K. M. (2015). Ambient noise tomography across the southern Alaskan Cordillera. *Geophys. Res. Lett. 42*, 3218–3227, doi: 10.1002/2015GL063613.

Ward, K. M. and F.-C. Lin (2018). Lithospheric structure across the Alaskan cordillera from the joint inversion of surface waves and receiver functions. *J. Geophys. Res. Solid Earth 123*, 8780–8797, doi: 10.1029/2018JB015967.

Watkins, W. D., C. H. Thurber, E. R. Abbott, and M. R. Brudzinski (2018). Local earthquake tomography of the Jalisco, Mexico region. *Tectonophysics 724-725*, 51–64, doi: 10.1016/j.tecto.2018.01.002.

Zhang, H., C. H. Thurber, D. Shelly, S. Ide, G. C. Beroza, and A. Hasegawa (2004). High-resolution subducting-slab structure beneath northern Honshu, Japan, revealed by double-difference tomography. *Geology 32*(4), 361–364, doi: 10.1130/G20261.1;.

Zhao, D., D. Christensen, and H. Pulpan (1995). Tomographic imaging of the Alaska subduction zone. *J. Geophys. Res. 100*(B4), 6487–6504.

Department of Geoscience
University of Wisconsin-Madison
1215 W. Dayton St.
Madison, USA WI 53706
(A.N., C.H.T.)
Department of Earth and Planetary Sciences,
University of California, Davis
One Shields ave, Davis, CA 95616,
and GNS Science
Dunedin, New Zealand
(D.E.P)
University of Alaska Fairbanks, Geophysical Institute
2156 Koyukuk Drive
Fairbanks, Alaska, U.S.A. 99775
(N.R., C.T., D.H.C.)
Department of Earth, Atmospheric and Planetary Sciences

Massachusetts Institute of Technology
Cambridge, MA, U.S.A. 02139
(H.F.)
University of North Alabama
Department of Physics and Earth Science
UNA Box 5172
Florence, Alabama 35632
(M.D.)
Department of Earth and Atmospheric Sciences
Cornell University
Ithaca, NY 14853
(G.A.A.)

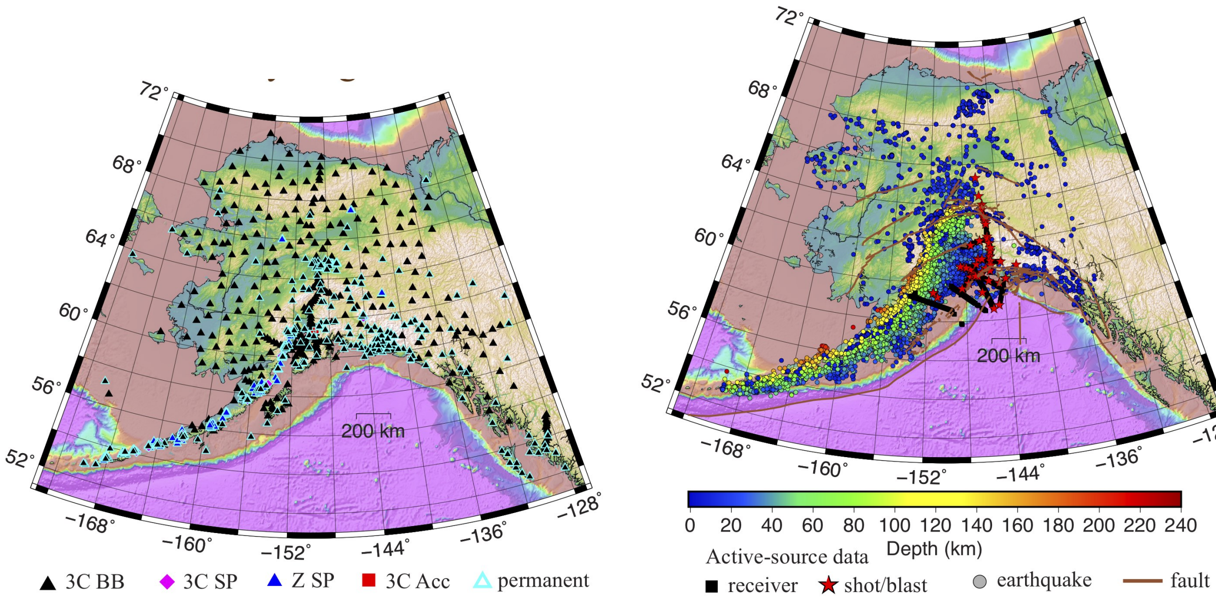

Figure 1. (a) Map of stations used for the assembly of our body-wave and surface-wave datasets. (b) Map of earthquakes (circles, color-coded by depth) and explosions (red stars) included in our body-wave dataset.

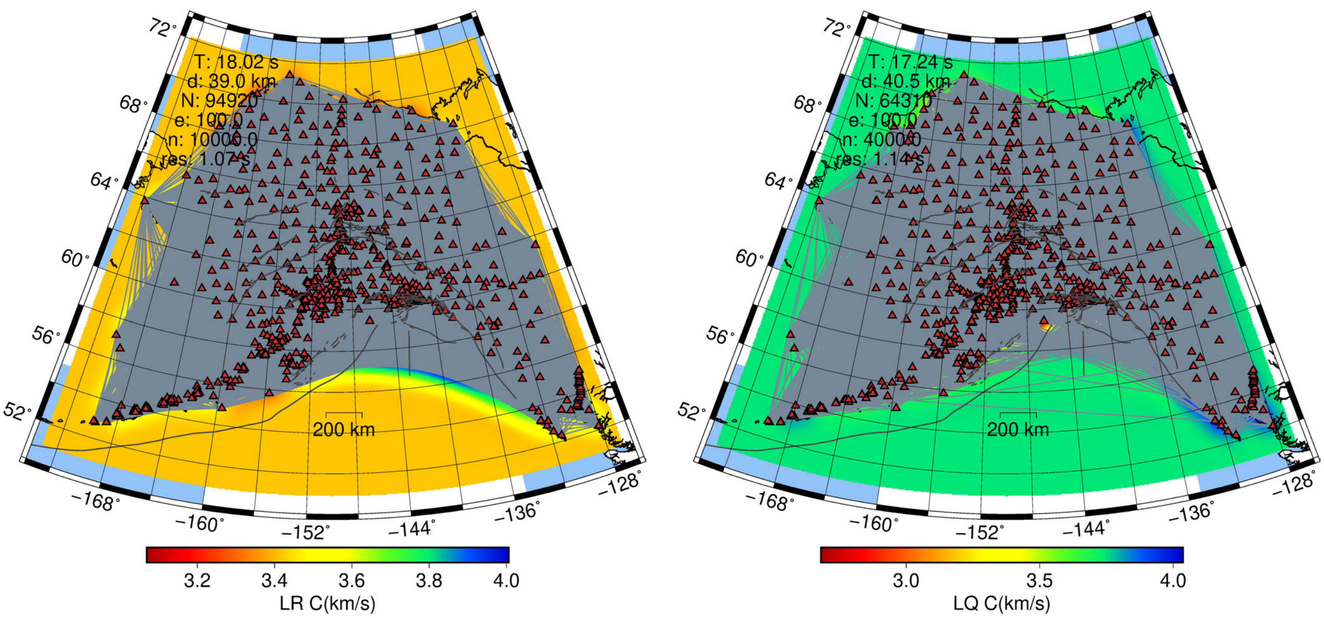

Figure 2. Example ray coverage maps for (a) Rayleigh waves at 18 s and (b) Love waves at 17 s.

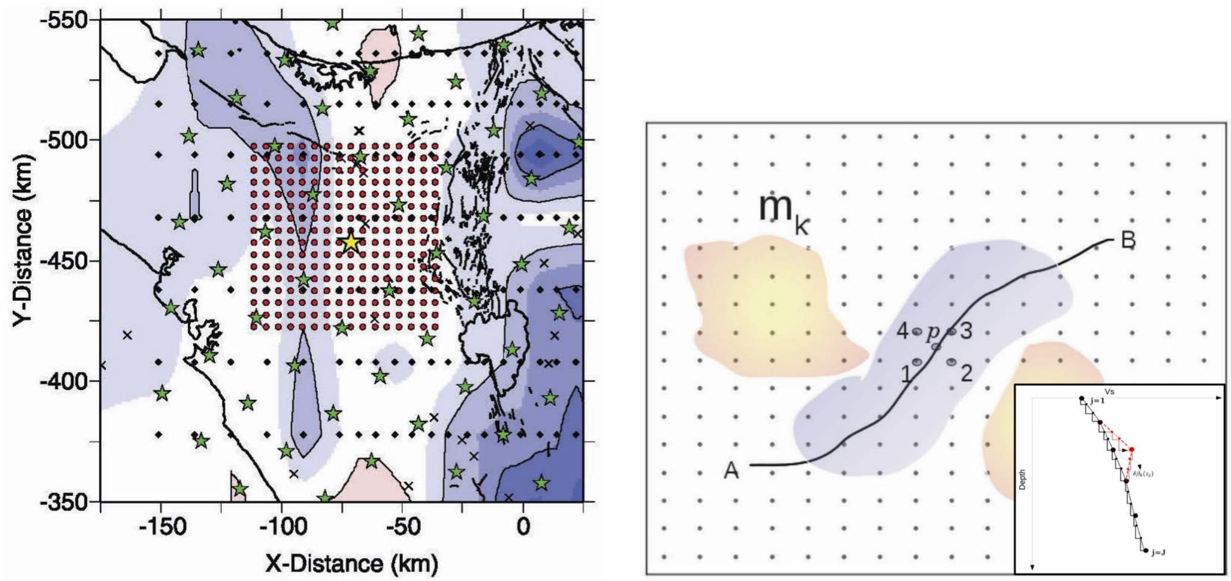

Figure 3. (a) Map view of part of the NZ-wide velocity grid, showing example of a box for computing group velocity partial derivatives at points (red dots) in a volume surrounding a group velocity observation (yellow star), analogous to points along a ray path from an earthquake travel-time. Small dots are 3-D velocity grid nodes, stars are other group velocity observation locations. From Eberhart-Phillips and Fry (2017). (b) Illustration of the Fang *et al.* (2015) sensitivity kernel calculation. The black solid line represents the propagation path between two stations A and B for the surface wave at some period. The phase slowness at any point p along the path is determined from the values at four surrounding horizontal grid points using a bilinear interpolation method for all available frequencies. Vs sensitivity kernels are then computed for discretized points and interpolated onto the surrounding nodes at discretized depths - see inset at lower right. From Fang *et al.* (2015).

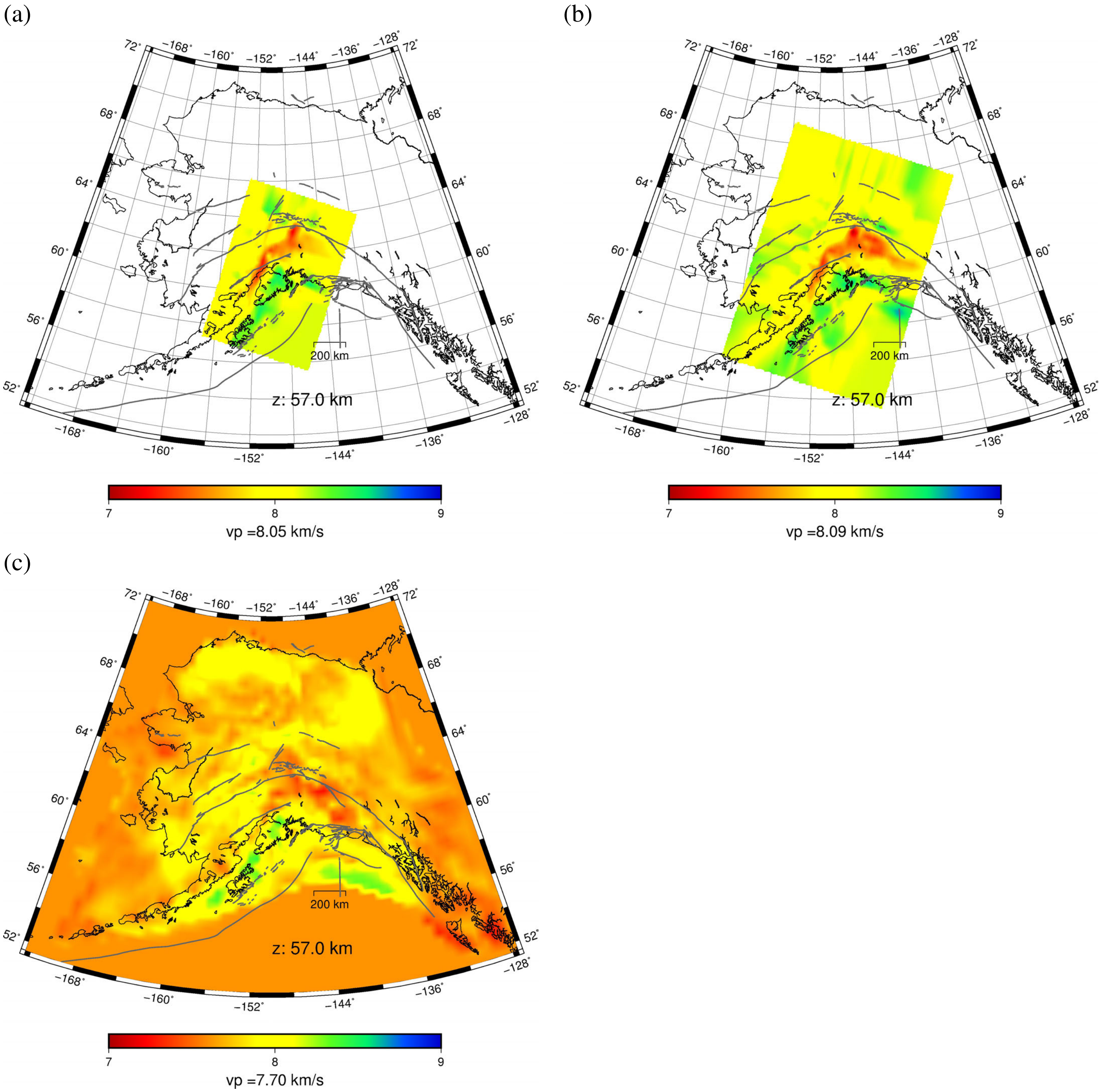

Figure 4. Map-view slices at 57 km depth through the Vp models (a) AKEP2006, (b) AKEP2020, and (c) AKAN2020. In the regions covered in common, the main features are generally consistent, although the absolute velocities are slightly lower on average in AKAN2020, as indicated by the average Vp at this depth indicated below the color bar. Vp values in km/s.

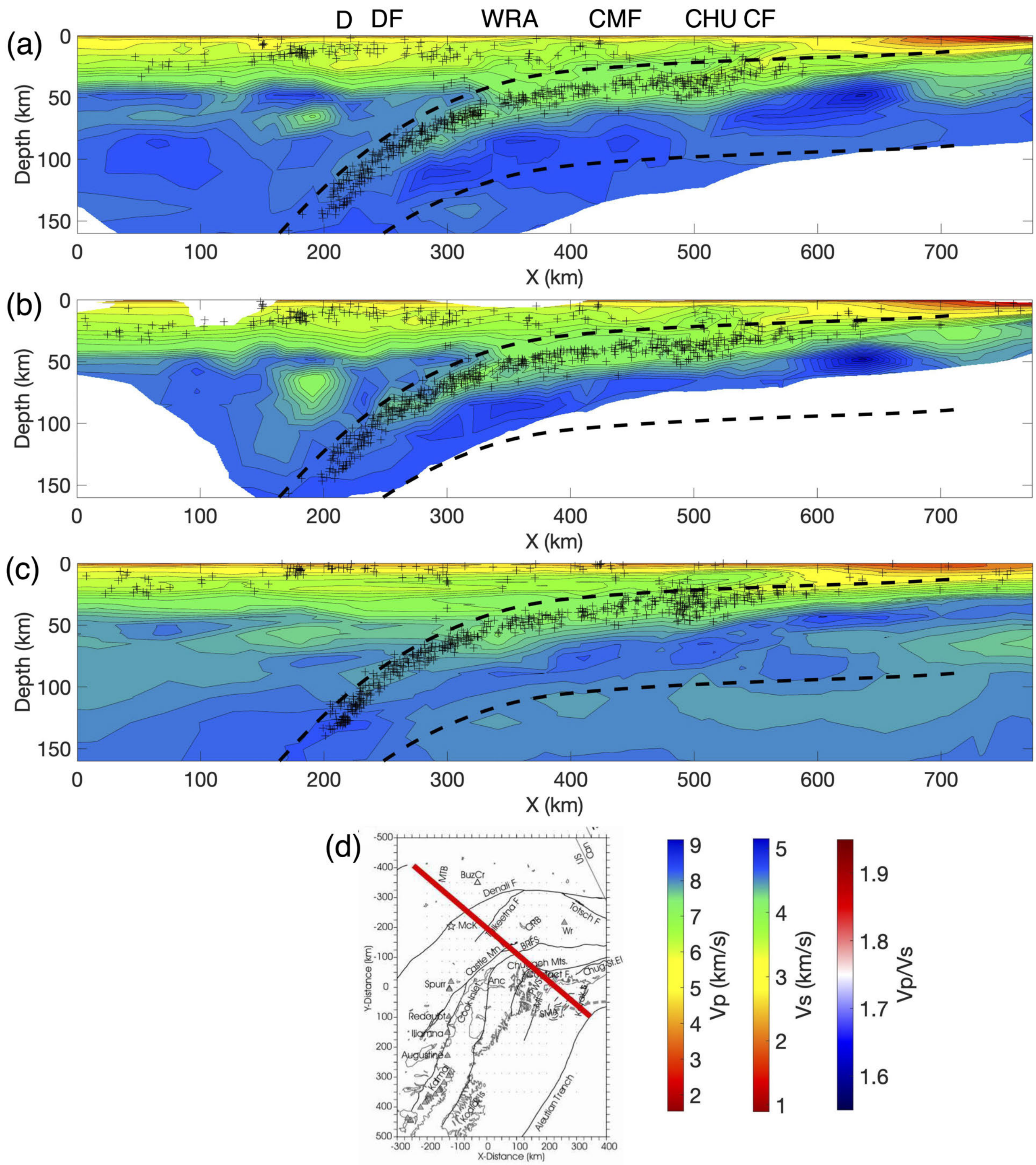

Figure 5. Cross-sections through Vp models (a) AKEP2020, (b) AKEP2006, and (c) AKAN2020 along the profile show in (d). D, Denali; DF, Denali fault; WRA, Wrangellia terrane; CMF, Castle Mountain fault; CHU, Chugach Mountains; CF, Contact fault. Slab top and bottom from Hayes *et al*. (2018) are shown by the black dashed lines. Color legends for Vp (here), Vs (Figure 6), and Vp/Vs (Figure 6) are shown in (d).

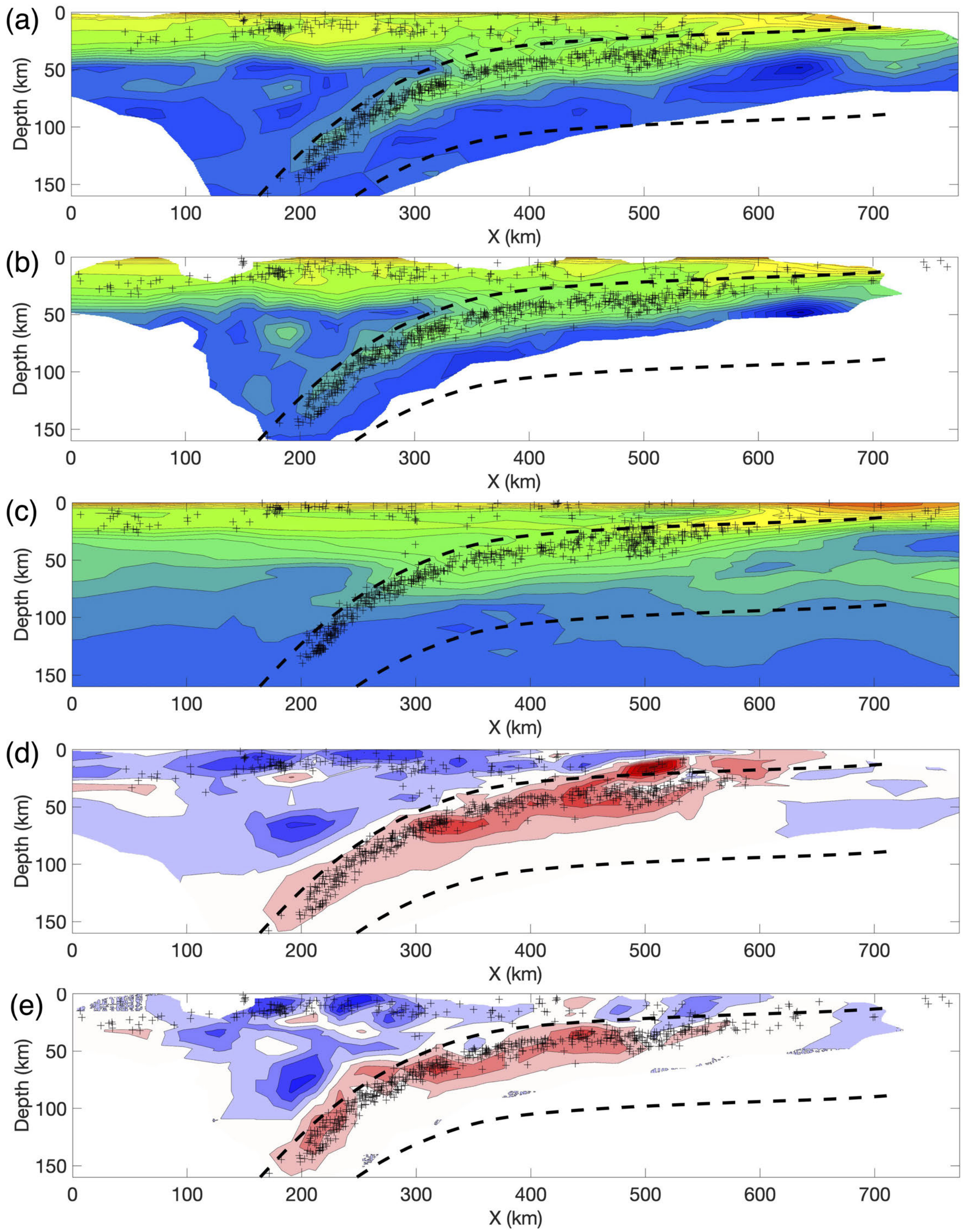

Figure 6. Cross-sections through Vs models (a) AKEP2020, (b) AKEP2006, and (c) AKAN2020, and Vp/Vs models (d) AKEP2020 and (e) AKEP2006 along the profile show in (f). D, Denali; DF, Denali fault; WRA, Wrangellia terrane; CMF, Castle Mountain fault; CHU, Chugach Mountains; CF, Contact fault. Slab top and bottom from Hayes *et al*. (2018) are shown by the black dashed lines. The cross section profile and color legends are shown in Figure 5d.

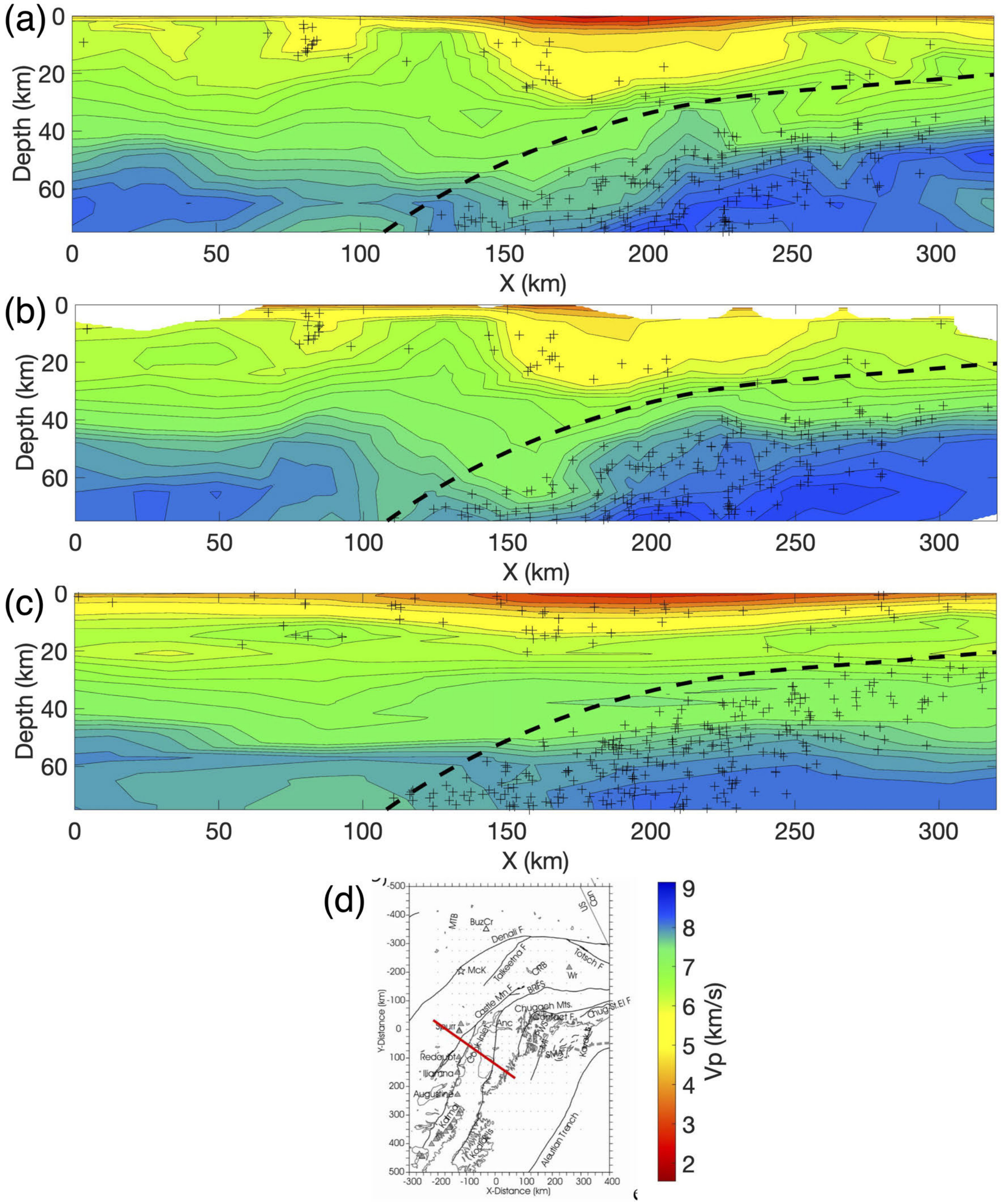

Figure 7. Cross-sections through Vp models (a) AKEP2020, (b) AKEP2006, and (c) AKAN2020 through Cook Inlet, along the profile show in (d). The color legend is also shown in (d).

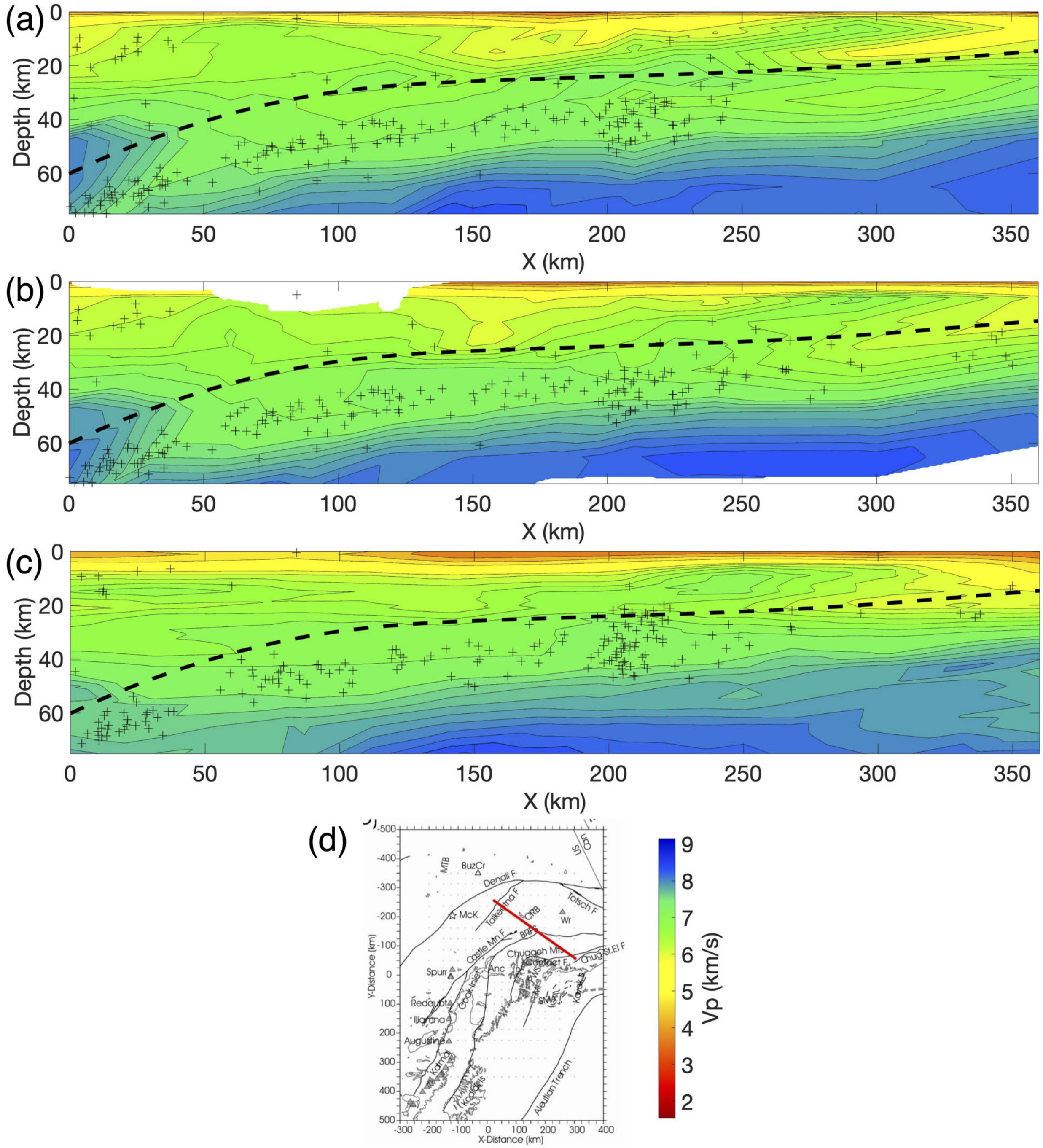

Figure 8. Cross-sections through Vp models (a) AKEP2020, (b) AKEP2006, and (c) AKAN2020 through the Copper River Basin, along the profile show in (d). The color legend is also shown in (d).

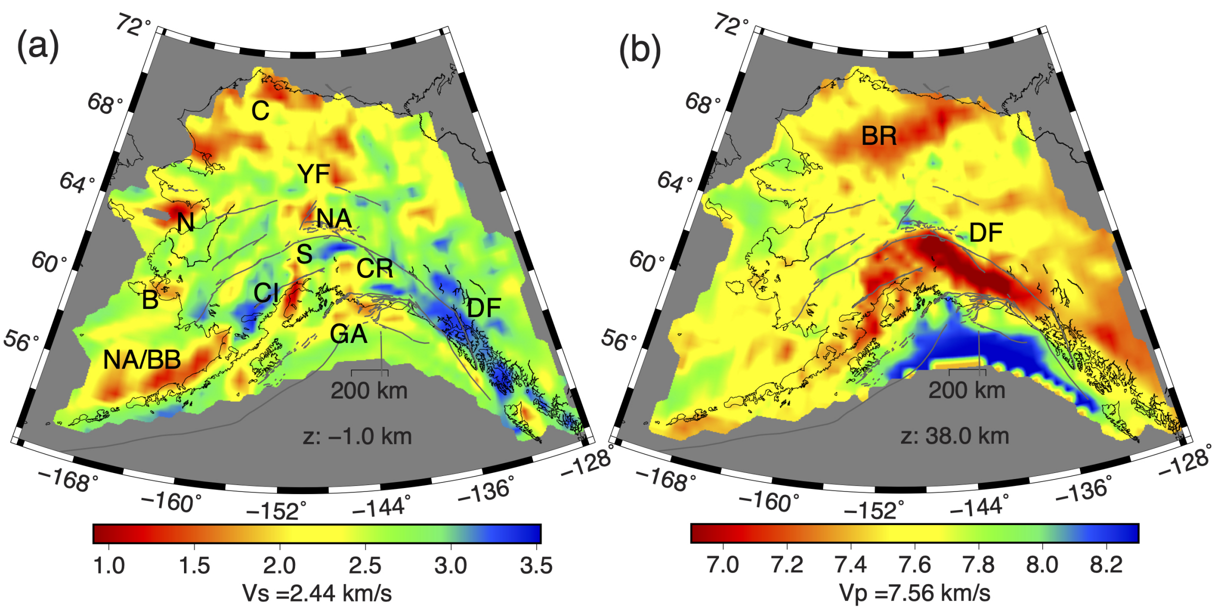

Figure 9. Depth slices for AKAN2020 (a) Vs at the reference depth and (b) Vp at depth 38 km. Features shown in the figures are: North Aleutian/Bristol Bay Basin (NA/BB), Bethel Basin (B), Cook Inlet Basin (CI), Susitna Basin (S), Gulf of Alaska (GA), Copper River Basin (CR), Denali Fault (DF), Nenana Basin (NA), Norton Basin (N), Yukon Flats Basin (YF), Colville Basin (C) and Brooks Range (BR).

Supplemental Information for: Three-Dimensional Seismic Velocity Models for Alaska from Joint Tomographic Inversion of Body-Wave and Surface-Wave Data

Avinash Nayak, Donna Eberhart-Phillips, Natalia Ruppert, Hongjian Fang, Melissa M. Moore, Carl Tape, Douglas H. Christensen, Geoffrey A. Abers, Clifford Thurber

June 9, 2020

S1 Additional technical details on the inversions

We tested a range of smoothing and damping parameters for the inversion of group velocity and phase velocity maps. In the inversion of surface-wave dispersion curves for 1D Vs models, we impose model smoothing and greater damping for deeper layers. In body-wave tomography, relative weights for P-wave and S-wave arrival times are 1.0 and 0.7, respectively. Additionally, weights decrease with epicentral distance from 1.0 at 100 km to $\sim$0.1 at the maximum distance ($\sim$900 km for P-wave and $\sim$600 km for S-wave picks). In the joint inversion for AKAN2020 model, the nodes are at depths (km): [-1:1 3:2:9 12:3:21 25:4:33 38:5:43 50:7:57 65 76 89 109 129 179 229 300].

S2 Seismic networks

Other networks used in this study are GM (USGS Network), II/IU (Global Seismograph Network), IM (International Miscellaneous Stations Network), NP (US National Strong-Motion Network), NY (Yukon-Northwest Seismic Network), US (US National Seismic Network), XF (Collaborative Research: Relating glacier-generated seismicity to ice motion, basal processes and iceberg calving), XF (Collaborative Research: Dynamic controls on tidewater glacier retreat), XM (Broadband recording at the site of great earthquake rupture in the Alaska Megathrust), XN (Collaborative Research: Canadian Northwest Seismic Experiment), XR (CSEDI: Observational and Theoretical Constraints on the Structure and Rotation of the Inner Core), XV (FLATS Fault Locations and Alaska Tectonics from Seismicity), XY (Magma Accretion and the Formation of Batholiths), XZ (STEEP Collaborative Research: St. Elias Erosion/Tectonics Project), YM (Columbia Glacier Passive Seismic Experiment), YV (Bering Glacier Surge Seismic Experiment), YV (MOOS Multidisciplinary Observations Of Subduction), ZQ (Taku Glacier), ZR (Bering Glacier Field Camp 2008), 5C (Dynamics of Lake-Calving Glaciers: Yakutat Glacier, Alaska) and station MM04 from 7C (The Mackenzie Mountains Transect: Active Deformation from Margin to Craton).

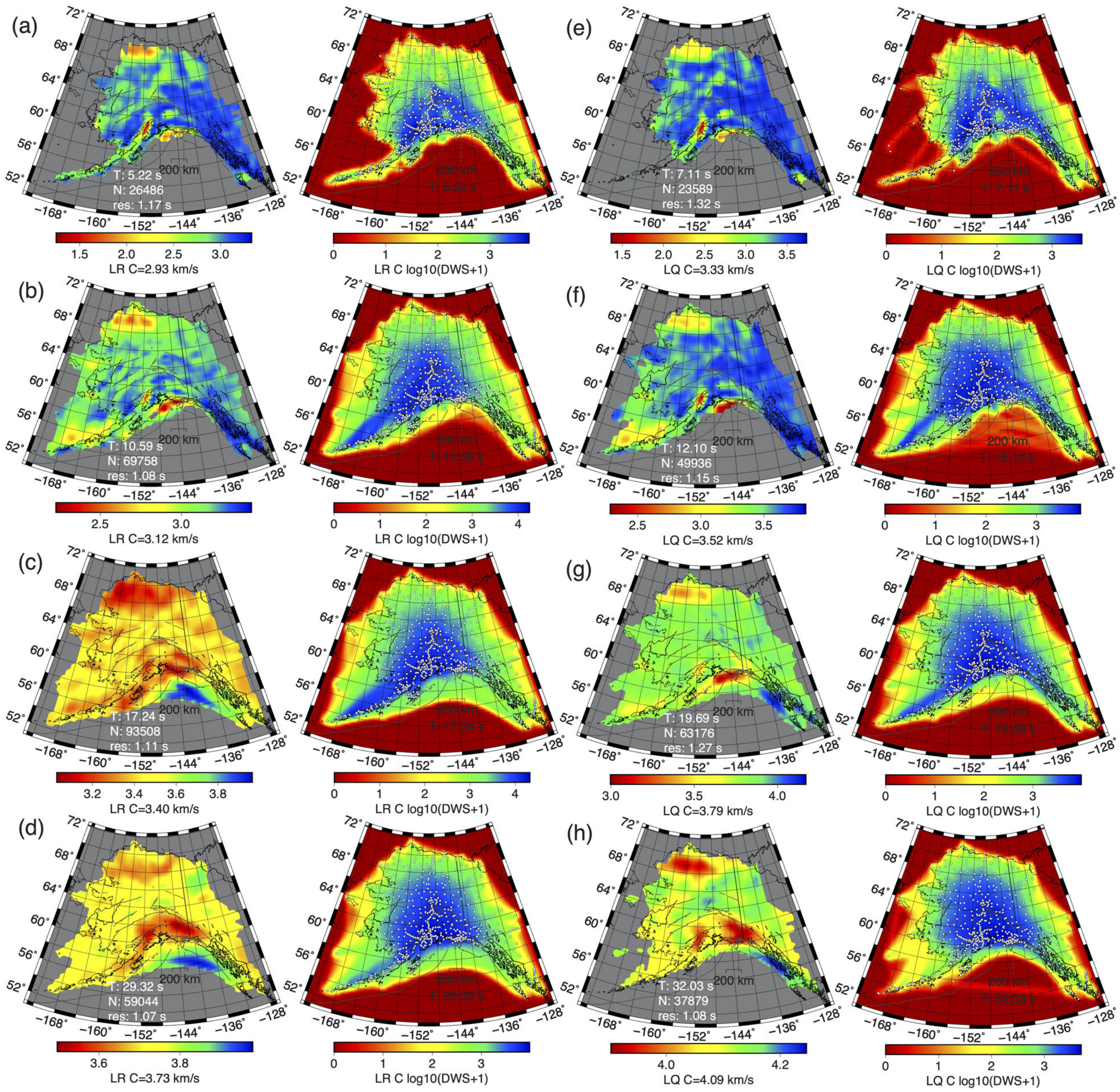

Figure S1: Surface-phase velocity maps and Derivative Weighted Sum (DWS) on a log10 scale for the statewide velocity model of Alaska. Columns from left to right are Rayleigh-wave phase velocity (LR C) maps, DWS for Rayleigh-wave phase velocity, Love-wave phase velocity maps (LQ C) and DWS for Love-wave phase velocity. Different rows are different periods ($\sim$5.2 s, $\sim$10.6 s, $\sim$17.2 s, $\sim$29.3 s for Rayleigh waves and $\sim$7.1 s, $\sim$12.1 s, $\sim$19.7 s, $\sim$32.0 s for Love waves from top to bottom). The period (T), number of measurements (N) and final weighted RMS phase arrival time misfit in seconds (res) are indicated on each phase velocity map. Areas with DWS $\leq$ 100 or log10(DWS+1) $\leq$ 2 are masked. White circles in DWS maps are stations used for that period.

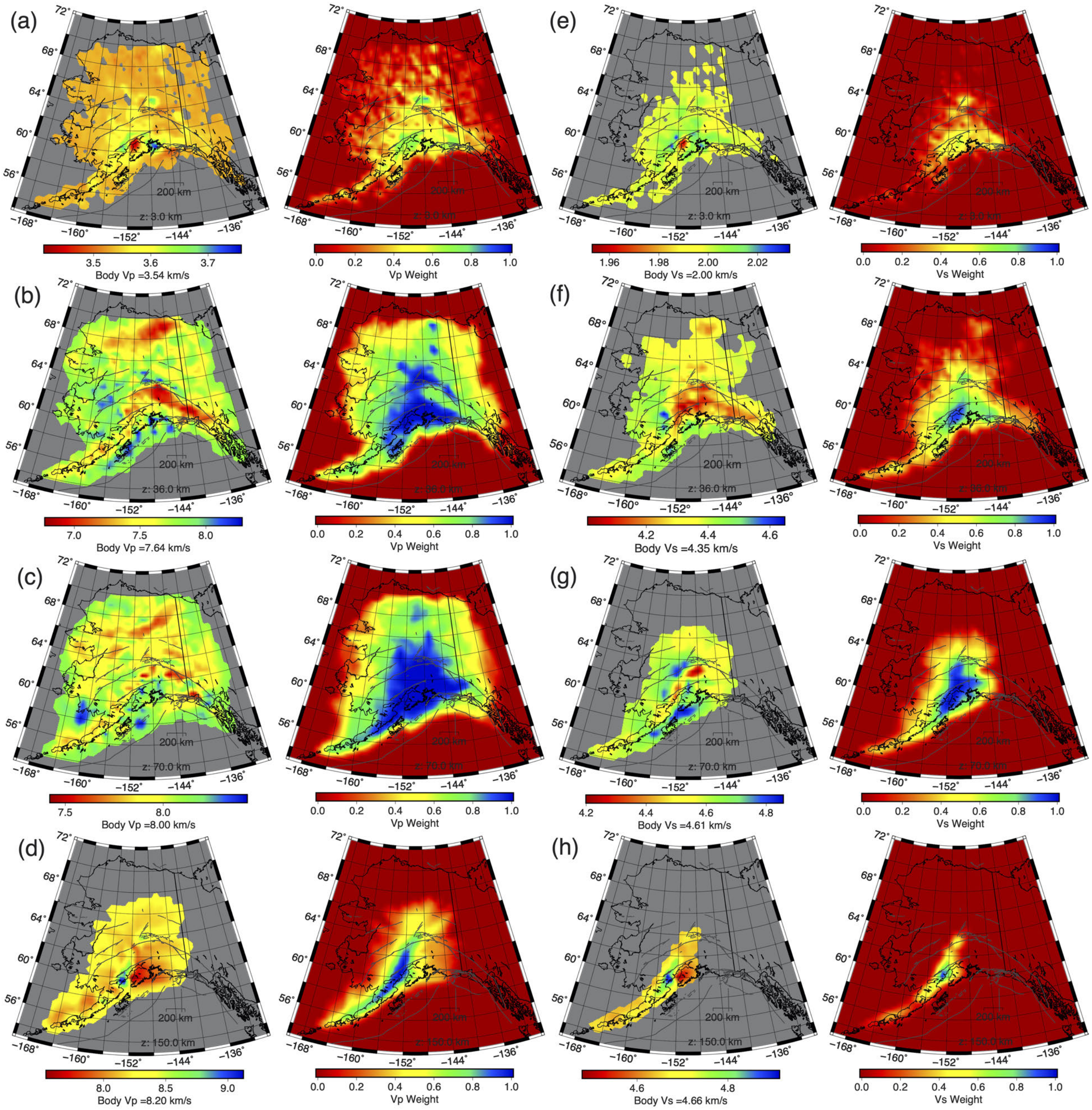

Figure S2: Body-wave tomography results for the statewide model of Alaska. The columns from left to right are Vp, rescaled DWS for Vp, Vs, and rescaled DWS for Vs. Different rows are different depths ($\sim$3 km, $\sim$36 km, $\sim$70 km and $\sim$150 km). DWS values are scaled from a range of 100–10000 to 0–1. Regions with DWS values $\leq$100 or rescaled weight $\leq$0.0 are masked.

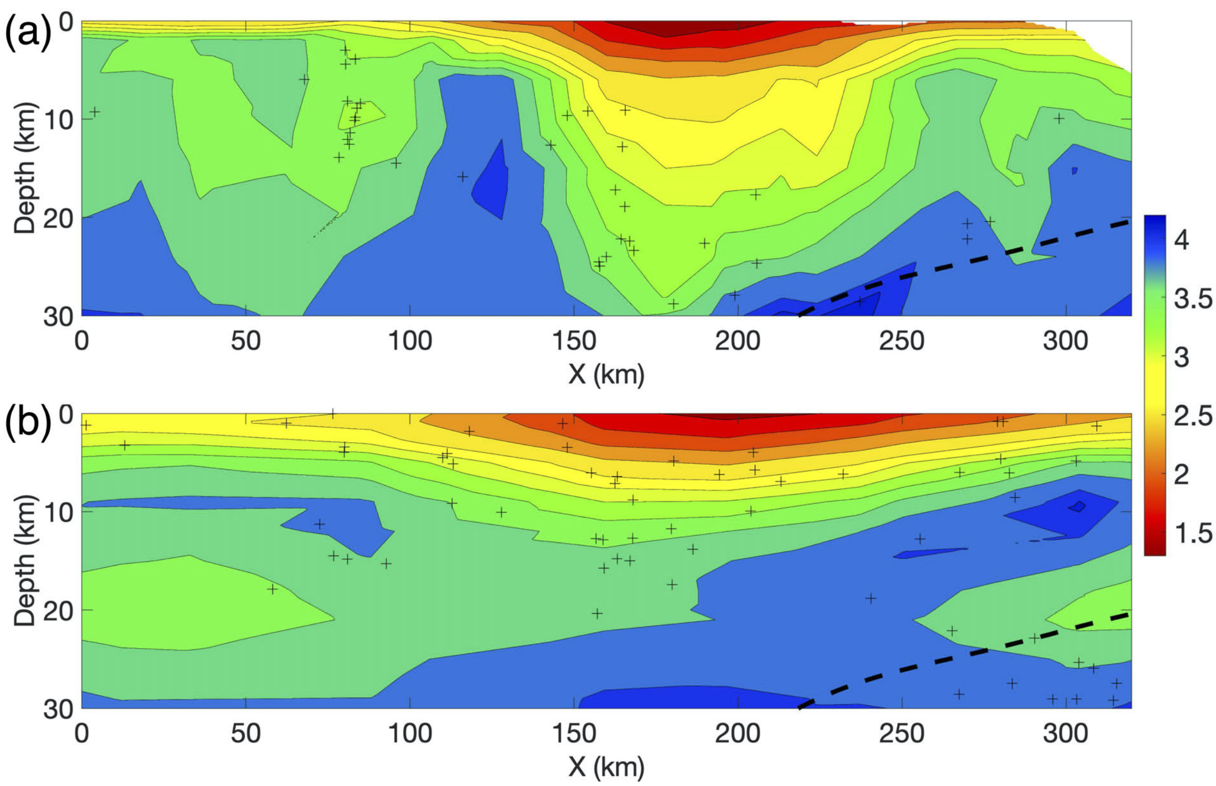

Figure S3: Cross-sections through Vs models (a) AKEP2020, (b) AKAN2020 through Cook Inlet, along the profile show in Figure 7d. Vertical exaggeration = 3.

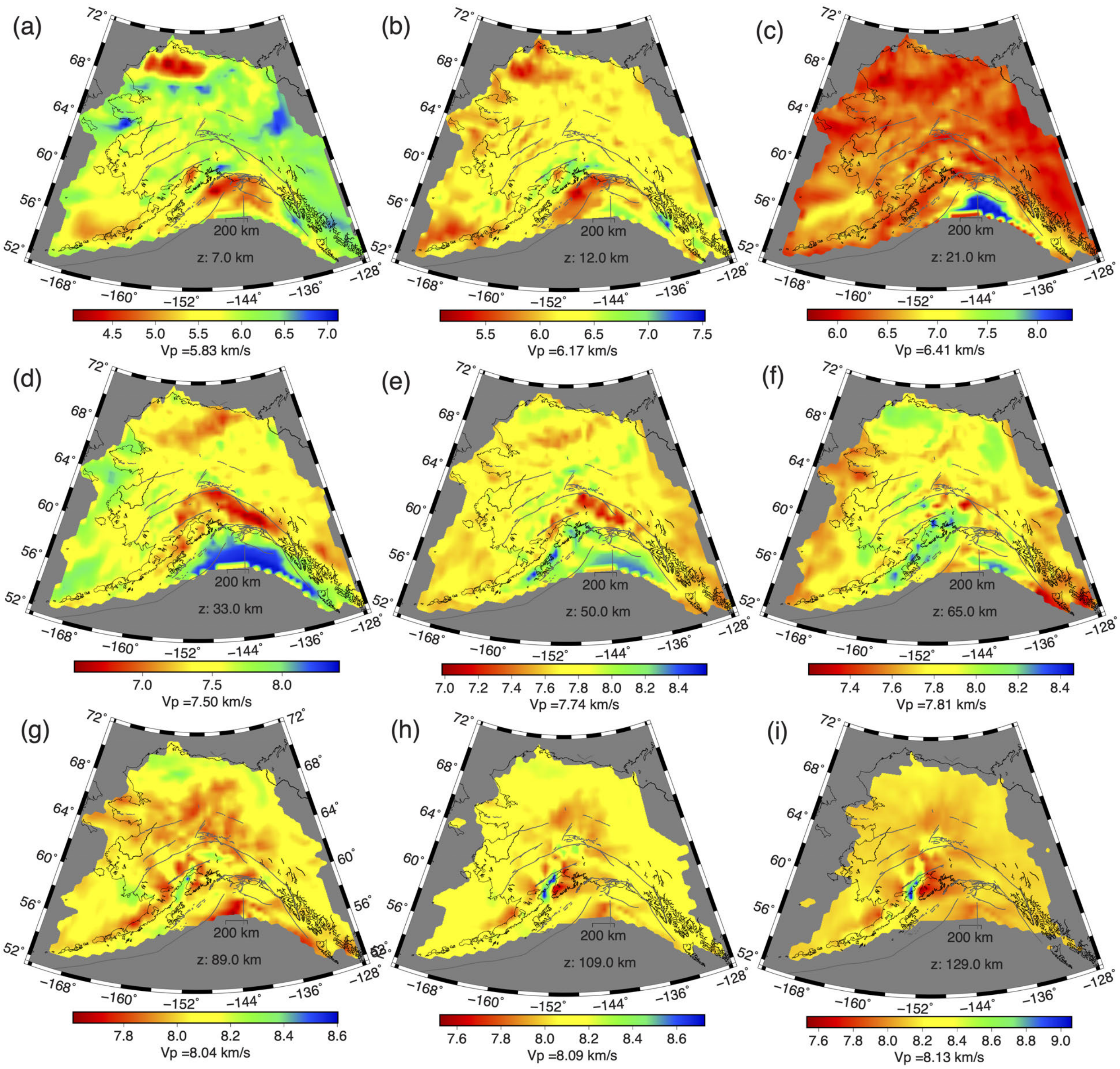

Figure S4: Vp depth slices for AKAN2020. Depths are indicated on each plot.

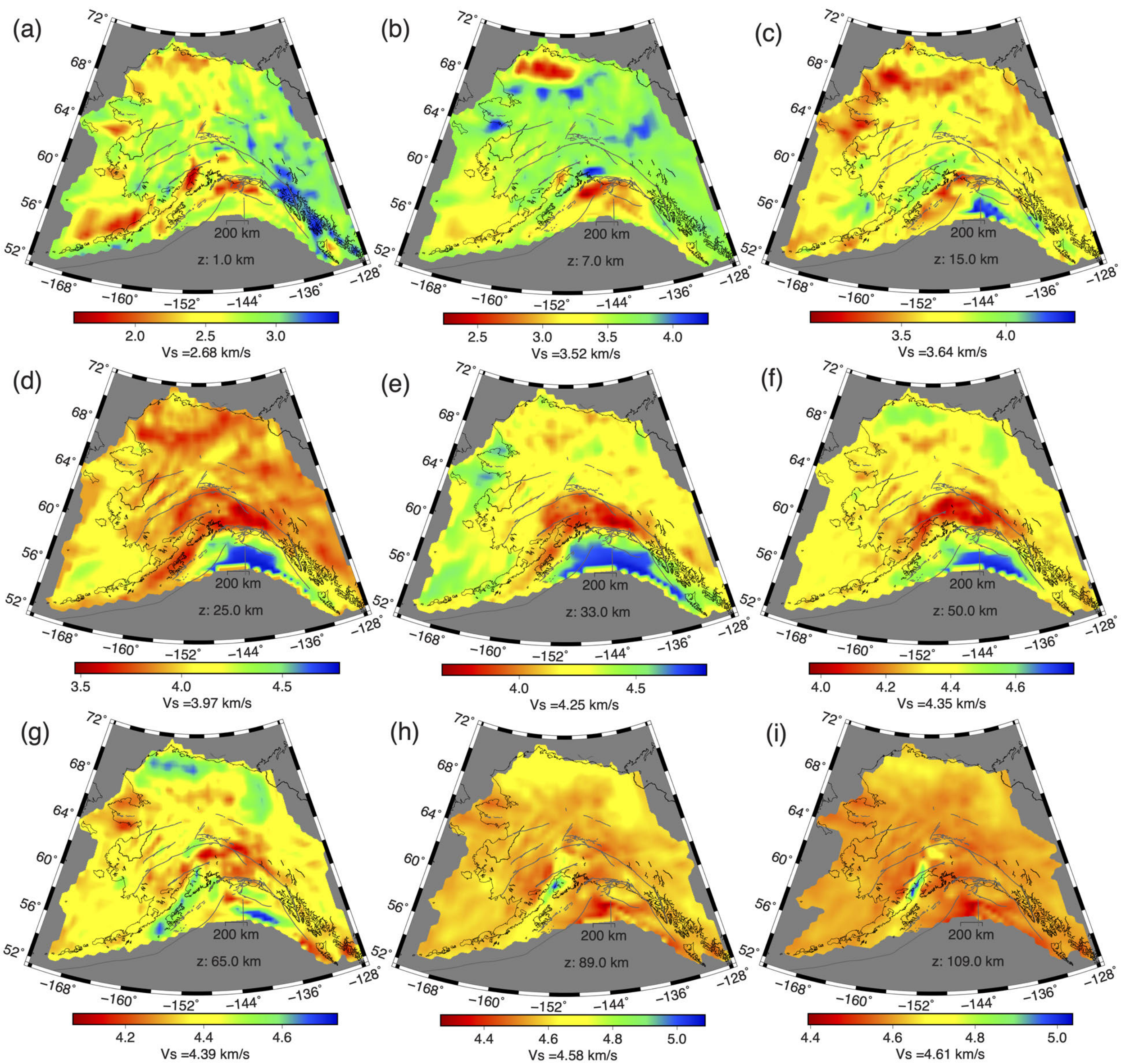

Figure S5: Vs depth slices for AKAN2020. Depths are indicated on each plot.